Compositional segregation in shaped Pt alloy nanoparticles and their structural behaviour during electrocatalysis

Article *in* Nature Materials · June 2013

DOI: 10.1038/nmat3668 · Source: PubMed

5 authors, including:

Chunhua Cui
University of Zurich
56 PUBLICATIONS **1,673** CITATIONS
SEE PROFILE

Lin Gan
Graduate School at Shenzhen, Tsinghua Univ…
38 PUBLICATIONS **1,236** CITATIONS
SEE PROFILE

Stefan Rudi
Forschungszentrum Jülich, Projektträger Jüli…
22 PUBLICATIONS **457** CITATIONS
SEE PROFILE

nature materials

ARTICLES

PUBLISHED ONLINE: 16 JUNE 2013 | DOI: 10.1038/NMAT3668

Compositional segregation in shaped Pt alloy nanoparticles and their structural behaviour during electrocatalysis

Chunhua Cui[1], Lin Gan[1], Marc Heggen[2], Stefan Rudi[1] and Peter Strasser[1]*

Shape-selective monometallic nanocatalysts offer activity benefits based on structural sensitivity and high surface area. In bimetallic nanoalloys with well-defined shape, site-dependent metal surface segregation additionally affects the catalytic activity and stability. However, segregation on shaped alloy nanocatalysts and their atomic-scale evolution is largely unexplored. Exemplified by three octahedral Pt_xNi_{1-x} alloy nanoparticle electrocatalysts with unique activity for the oxygen reduction reaction at fuel cell cathodes, we reveal an unexpected compositional segregation structure across the {111} facets using aberration-corrected scanning transmission electron microscopy and electron energy-loss spectroscopy. In contrast to theoretical predictions, the pristine Pt_xNi_{1-x} nano-octahedra feature a Pt-rich frame along their edges and corners, whereas their Ni atoms are preferentially segregated in their {111} facet region. We follow their morphological and compositional evolution in electrochemical environments and correlate this with their exceptional catalytic activity. The octahedra preferentially leach in their facet centres and evolve into 'concave octahedra'. More generally, the segregation and leaching mechanisms revealed here highlight the complexity with which shape-selective nanoalloys form and evolve under reactive conditions.

The identification of materials that can efficiently electro-catalyse oxygen surface chemistry remains a key challenge for the design of a number of important future electrochemical conversion and storage devices, such as conventional and regenerable fuel cells, Li-air batteries, or electrolysers[1–3]. In particular, the sluggish oxygen reduction reaction (ORR) on Pt limits the performance of low-temperature polymer electrolyte membrane fuel cells[4–8]. One of the approaches to improve the catalytic kinetics is alloying Pt with early, such as Sc or Y, or late, such as Fe, Co and Ni, transition metals[9–12]. After the discovery of the exceptionally ORR active $Pt_3Ni(111)$ surface, characterized by a segregated single Pt surface layer associated with a distinctive shift in the electronic Pt valence *d* bands (called Pt 'skin' surface-sandwich structure)[13,14], much effort was dedicated to the synthesis and electrochemical investigation of octahedral skin Pt–Ni nanoparticles[15–19]. Owing to their exclusive (111)-oriented facets they were predicted to be 'dream' ORR catalysts[20].

There is no *a priori* reason that would preclude the formation of an electronic surface structure similar to that found in $Pt_3Ni(111)$ skins alloys through other means than thermal segregation of a single Pt layer from a $Pt_3Ni(111)$ facet. Indeed, multiple (111)-oriented Pt surface layers in combination with Pt-poor subsurface cores may give rise to surface lattice strain resulting in comparable *d*-band shifts and favourable oxygen electrocatalysis[21–23]. Such core–shell structures are accessible by preferential chemical or electrochemical leaching (dealloying) of a non-noble alloy component, for example Ni, in acid or during electrode potential cycling, respectively[24–29]; their shell thickness can be controlled by the cycling conditions and initial alloy composition[21,30]. Hence, dealloyed Pt–Ni octahedra allow an optimization of the surface electronic structure to maximize their ORR activity, yet there has been virtually no effort to vary their bulk and surface composition and relate them to the observed catalytic activity and stability. Monte Carlo simulations have predicted a Pt skin 'surface-sandwich' structure for Pt–Ni nanoparticles regardless of their shape and composition[31], yet experimental data on the composition distribution in shaped Pt alloy nanoparticles and their evolution under reactive conditions are so far missing. Given the fact that such bimetallic octahedral Pt–Ni skin particles would represent the most active ORR catalysts ever designed, it is imperative to fill that knowledge gap.

We report the discovery of unusual compositional patterns inside pristine Pt_xNi_{1-x} nano-octahedra, follow their distinct morphological and compositional evolution trajectories with atomic-scale resolution during electrochemical potential cycling, reveal surprising morphologies in shaped particles and correlate these with their surface electrocatalytic ORR activity. We achieve this by using probe-corrected scanning transmission electron microscopy and electron energy-loss spectroscopy (STEM-EELS). Our study involves Pt alloy octahedra with three distinct initial Pt_xNi_{1-x} bulk compositions, in particular $Pt_{1.5}Ni$, PtNi and $PtNi_{1.5}$, to realize a wide range of near-surface compositions during the electrochemical treatments. Our insights establish that nanoscale Pt_xNi_{1-x} octahedra feature a Pt-rich frame along their edges and corners, and their Ni atoms are preferentially segregated in their {111} facets. As a result of this, we show that the octahedra preferentially leach in their Ni-rich {111} facet centres and evolve into 'concave nano octahedra'. The degree of 'concaveness' varies with the initial Ni content in the bulk. Our new atomic insights provide a clearer picture on the viability of the octahedral Pt–Ni alleged 'dream' ORR electrocatalysts.

[1]The Electrochemical Energy, Catalysis, and Materials Science Laboratory, Department of Chemistry, Chemical Engineering Division, Technical University Berlin, Berlin 10623, Germany, [2]Ernst Ruska-Centre for Microscopy and Spectroscopy with Electrons, Forschungszentrum Juelich GmbH, 52425 Juelich, Germany. *e-mail: pstrasser@tu-berlin.de

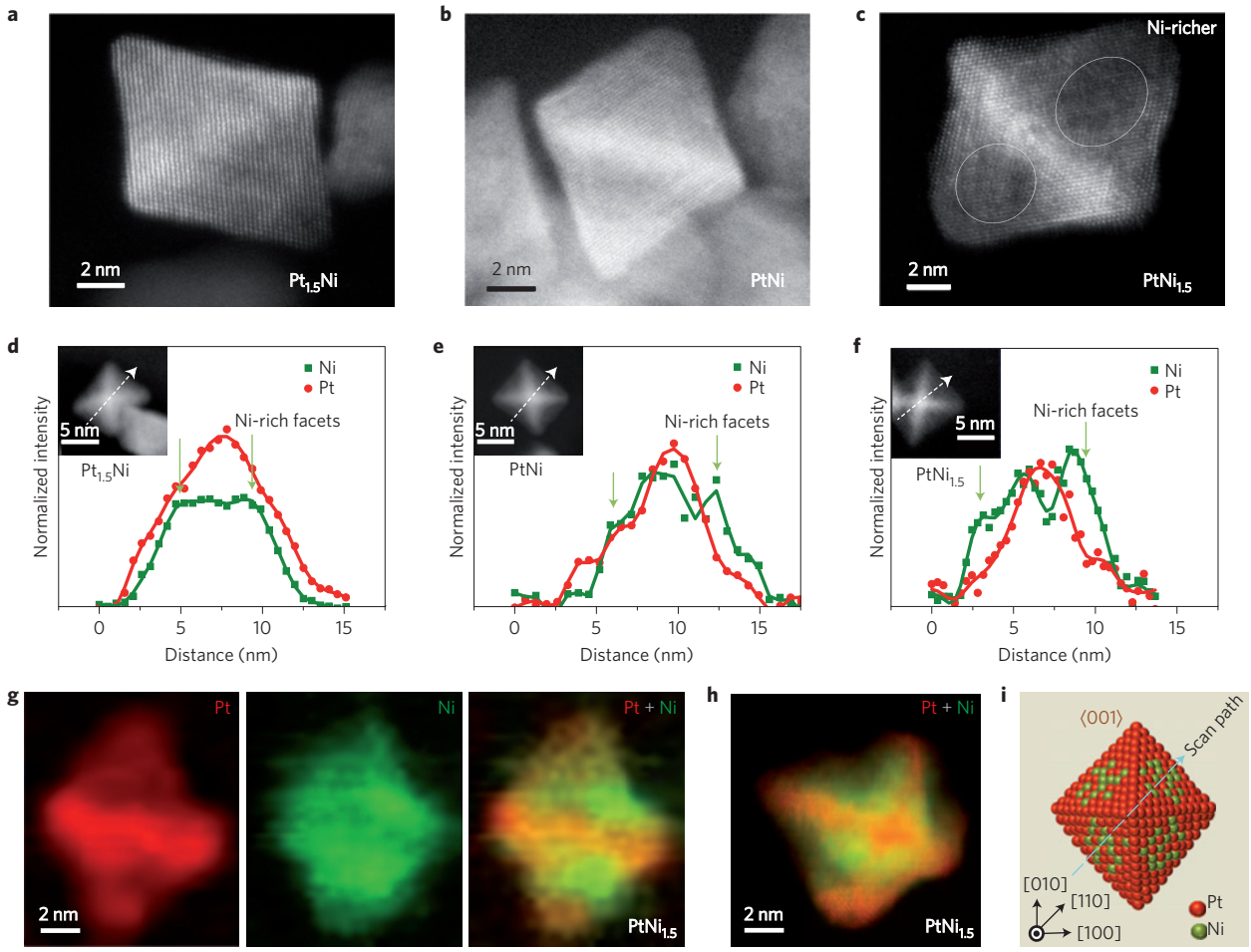

Figure 1 | Atomic-scale *Z*-contrast STEM images and composition profile analysis of Pt_xNi_{1-x} octahedral nanoparticles. a–c, *Z*-contrast STEM images of $Pt_{1.5}Ni$ (**a**), PtNi (**b**) and $PtNi_{1.5}$ (**c**) octahedral nanparticles close to the ⟨110⟩ zone axis. **d–f**, EELS line scan analysis of of $Pt_{1.5}Ni$, PtNi and $PtNi_{1.5}$ octahedral nanoparticles close to the ⟨100⟩ zone axis, respectively. The scan path is specified along the [110] direction passing through the longest major axis to track the Ni composition profile. The insets are the *Z*-contrast images of a corresponding single nanoparticle. Further information can be found in Supplementary Fig. S3. **g**, EELS element map of $PtNi_{1.5}$ shows the segregated distribution of Pt (red) and Ni (green) in a particle close to the ⟨110⟩ zone axis. **h**, Composite image of a HAADF image showing mainly Pt (red) and an EELS map showing Ni (green) in a particle close to the ⟨100⟩ zone axis. **i**, Ball schematic sketch shows the particle model along the ⟨001⟩ zone axis and the Ni-rich facet profile and Pt-rich frame.

Octahedral $Pt_{1.5}Ni$, PtNi and $PtNi_{1.5}$ nanoparticles were prepared using a dimethylformamide-based solvothermal method at 120 °C (see Supplementary Information). The bulk compositions of the three samples were controlled by adjusting the initial Pt and Ni precursor ratios. Their bulk composition was determined by inductively coupled plasma mass spectrometry and energy-dispersive X-ray spectra, respectively. Transmission electron microscopy (TEM) images (see Supplementary Fig. S1) evidence their octahedral shape, enclosed by eight {111} facets. The particle size is 11 ± 0.9 nm for $Pt_{1.5}Ni$, 12 ± 0.8 nm for PtNi and 13 ± 1.2 nm for $PtNi_{1.5}$. Once supported on carbon, the crystal phases of the catalysts were measured by X-ray diffraction (XRD; Supplementary Fig. S2). The XRD patterns suggest a face-centred cubic alloy structure. The (111) peak position shift reflects lattice contraction with more Ni content. Peak shoulders developed in PtNi and $PtNi_{1.5}$, suggesting segregated phases.

To clarify the morphology and composition profile of the as-prepared octahedral Pt_xNi_{1-x} nanoparticles at atomic-scale resolution, we studied a series of independent octahedral Pt_xNi_{1-x} nanoparticles in Fig. 1 and Supplementary Fig. S3 using a probe-corrected STEM (ref. 32). Figure 1a–c showed the atomic-scale high angle annular dark field (HAADF) STEM images (also known as *Z*-contrast images) of the Pt_xNi_{1-x} nanoparticles roughly oriented along the ⟨110⟩ zone axis, clearly demonstrating the octahedral morphology. Sharp *Z*-contrast images suggest non-uniform Ni distributions in Fig. 1b,c. For instance, the dark regions in the $PtNi_{1.5}$ nanoparticle (Fig. 1c) marked with white ellipses adjacent to the bright central region of the octahedron indicate a Ni-rich facet region. *Z*-contrasts are less pronounced for $Pt_{1.5}Ni$ (Fig. 1a). *Z*-contrasts of PtNi octahedra (Fig. 1b) suggest Pt-enriched edges and corners, adjacent to a Ni-rich facet region. To further evidence metal segregation, EELS line analysis was applied. As shown in Fig. 2d–f, the Pt and Ni composition distributions were studied in octahedral particles oriented along the ⟨100⟩ zone axes (see insets). Line scans along the ⟨110⟩ direction started and ended at the edges, passing through the central octahedron axis. The $Pt_{1.5}Ni$ sample demonstrated nearly symmetrical Pt and Ni EELS profiles, taking thickness variations into account; however, their relative intensities showed a clear Pt enrichment in the central axis compared to the facets. Line scans in Fig. 1e,f show that Pt and Ni metal enrichment in axis and facets, respectively, increased further with more bulk Ni. In the $PtNi_{1.5}$ sample, the facet Ni content was significantly larger than on the axis. The line scan results are consistent with the XRD patterns and reflect the *Z*-contrast images in the insets of Fig. 1d–f. The particles have well-faceted structures, where the bright cross represents the corner and edges. The four symmetrical

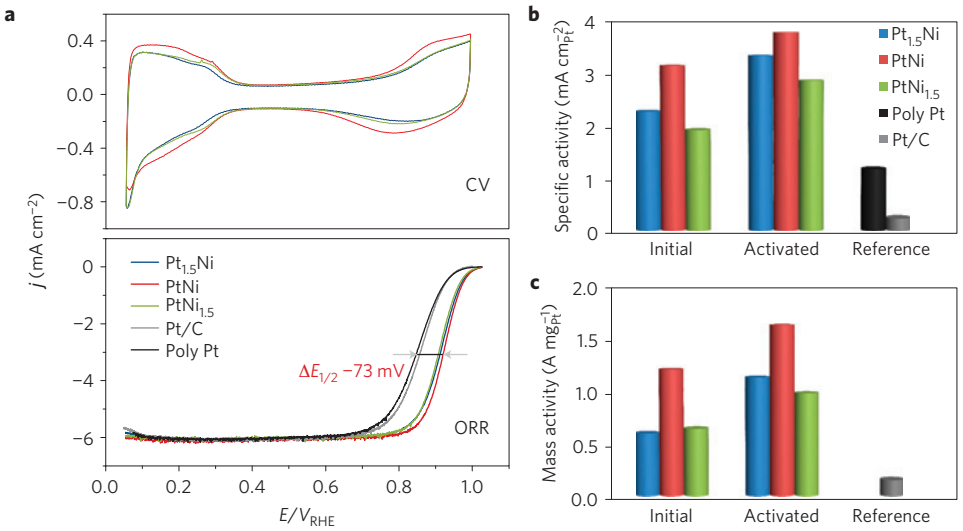

Figure 2 | Electrochemical studies on carbon-supported Pt_xNi_{1-x} octahedra. a, Cyclic voltammograms (CV) of Pt_xNi_{1-x} octahedra in 0.1 M $HClO_4$ solution at 25 °C (100 mV s^{-1}; top). ORR polarization curves of three Pt_xNi_{1-x} octahedra compared to commercial Pt/C and polycrystalline Pt were recorded in O_2 saturated 0.1 M $HClO_4$ solution at 25 °C with a sweep rate of 5 mV s^{-1} at 1,600 r.p.m. (bottom). ORR activity is evaluated at 0.9 V versus the reversible hydrogen electrode (RHE) potential. The mass and specific activities of commercial Pt/C at 0.9 V_{RHE} are ~0.15 A mg_{Pt}^{-1} and ~0.23 mA cm_{Pt}^{-2}. The specific activity of polycrystalline Pt is ~1.2 mA cm_{Pt}^{-2}. **b**,**c** Specific activity and mass activity, respectively, of Pt_xNi_{1-x} octahedra after different electrochemical processing. 'Initial' and 'activated' represent the carbon-supported Pt_xNi_{1-x} octahedral electrocatalysts after 3 and 25 potential cycles, respectively, in the potential region 0.06–1.0 V_{RHE} at a scan rate of 250 mV s^{-1}.

facets darken progressively from Fig. 1d–f, evidencing the relative enrichment in Ni. In regards to the composition of the surface, EELS scans of $Pt_{1.5}Ni$ showed Pt-rich facets of 2–4 atomic layers in thickness. Higher bulk Ni content in $PtNi_{1.5}$ resulted in facets with segregated Ni top layers of 4–7 atomic layers in thickness (Fig. 1f), whereas the PtNi sample shows a mixed facet alloy surface (Fig. 1e). The compositions in the corners and edges can be found in Supplementary Fig. S3. Supplementary Fig. S3c,f with their three distinct Pt maxima evidence Pt-rich axes and corners. Also, scans in ⟨110⟩-oriented particles (Supplementary Fig. S3d) demonstrated Pt-rich edges. The metal segregation characteristics revealed were further evidenced by the element maps of $PtNi_{1.5}$ in Fig. 1g,h. We conclude that the pristine Pt_xNi_{1-x} nano octahedra show a Pt-rich frame (corners and edges) and Ni-rich facet regions, which is schematically rendered in Fig. 1i. This is the first report of such an unusual metal segregation in a polyhedral alloy.

At electrode potentials where molecular oxygen starts to electroreduce, most bimetallic Pt alloys leach the less noble component from the surface. Pt–Ni is no exception. The pristine composition of the {111} facets of the three shaped catalysts ranged from Pt-rich to Ni-rich with increasing bulk atomic fraction of Ni. As a result of this, during electrode potential cycling in the range 0.06–1.0 V_{RHE} the catalysts dealloyed each in their characteristic way with different rates and to different extents, yielding a Pt overlayer of varying thickness and roughness[21]. We used this to monitor their ORR activity with increasing potential cycling and identified the number of cycles where the ORR activity of each catalyst peaked. The catalytic surface after three potential cycles was referred to as 'initial' (Fig. 2). After 25 potential cycles (referred to as the 'activated' state of the catalysts in Fig. 2), the ORR activities of the $Pt_{1.5}Ni$, PtNi and $PtNi_{1.5}$ electrocatalysts reached their maximum value.

Cyclic voltammetry of the activated catalysts (Fig. 2a top) showed typical Pt characteristics and served to evaluate the electrochemical surface area (ECSA) based on H_{upd} charge, Q_H. Also, CO adsorption and voltammetric stripping yielded the ECSA based on Q_{CO}. Polarization curves for the ORR for the three 'activated' catalysts are compared to high surface area carbon-supported commercial Pt/C catalyst and state-of-the-art polycrystalline Pt electrodes in Fig. 2a. The linear sweep voltammetry curves reveal that the ORR kinetic is dramatically accelerated on dealloyed octahedral Pt_xNi_{1-x} nanoparticles, especially on the dealloyed PtNi surface relative to polycrystalline Pt. A significant positive shift of 73 mV was observed in the half-wave potential, implying a significant increase of the ORR activity. As shown in Fig. 2b, the specific activity exhibits a significant increase for all three catalysts, suggesting the dealloyed surface on octahedral nanoparticles exhibits surface electronic properties favourable for the ORR (ref. 22). Our H_{upd} and CO stripping experiments confirmed that this ORR activity enhancement cannot be due to the formation of a surface Pt-skin structure, because the ratio between the surface charges $Q_{CO}/2Q_H$ is close to unity (Supplementary Fig. S4), ruling out the presence of the thermally segregated Pt skin structure with its characteristic ratio of 1.5 (ref. 33). The high ORR activities in Fig. 2b,c represent a factor of 6–10 increase in Pt mass activities and a factor of 10–15 increase in Pt specific activities relative to commercial carbon-supported Pt nanoparticle electrocatalysts, the highest ever reported precious metal group (PGM) mass activity value for carbon-supported Pt alloy electrocatalysts[15–18,26].

To get an insight into how the ORR activity trajectories of Pt_xNi_{1-x} octahedra correlate with structural, compositional and morphological changes, bulk compositional inductively coupled plasma analysis combined with atomic-scale TEM/STEM/EELS studies of the activated catalysts were performed. Surprisingly, all three activated Pt_xNi_{1-x} catalysts had changed their bulk composition to roughly Pt_3Ni (Supplementary Fig. S5). Considering the ORR activity difference of the activated catalysts (Fig. 2) the residual bulk Ni clearly seems to be an insufficient descriptor for ORR activity[26,34–36].

Supplementary Fig. S6 presents a synopsis of conventional TEM images of the three activated octahedral catalysts and gives initial evidence of unusual morphological transformations. Subsequent atomic-scale morphological and structural studies of the activated catalysts are reported in Fig. 3. EELS scans of the dealloyed PtNi (Fig. 3a,b) and $Pt_{1.5}Ni$ (Fig. 3d,e) confirm that 25 voltammetric potential cycles have leached out Ni atoms from the {111} facets to

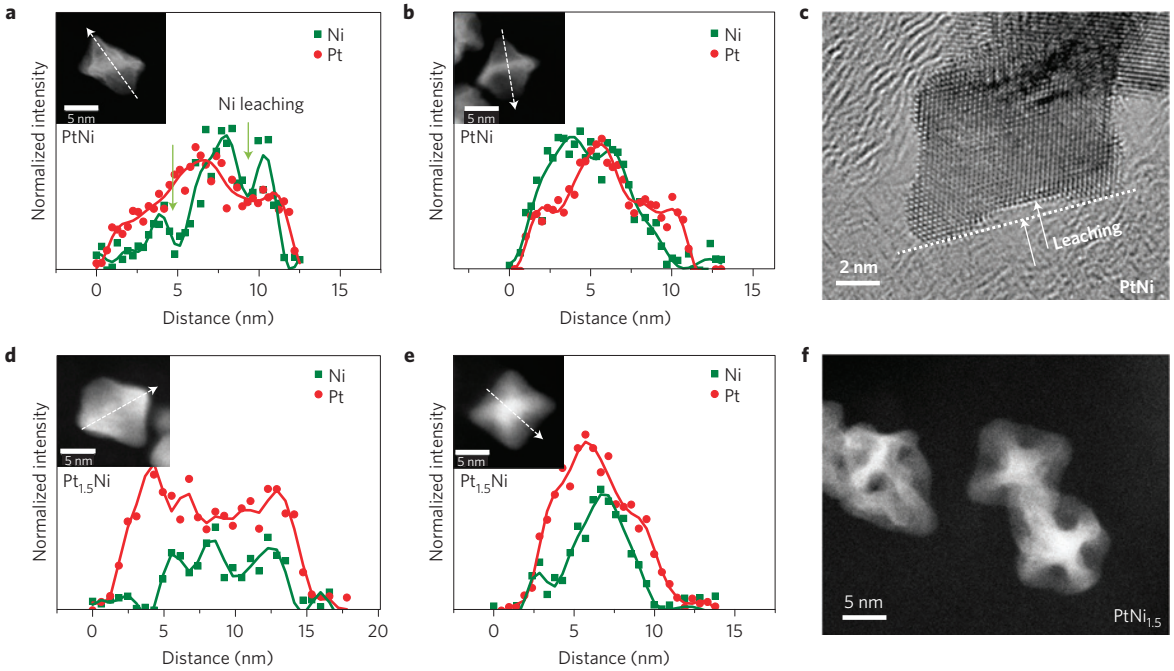

Figure 3 | STEM-EELS analysis of $Pt_{1.5}Ni$ and PtNi octahedra after 25 potential cycles. a,**b**, EELS line scans show the selective leaching of Ni in the facet region on PtNi. Pt rich corners were observed. The STEM images in the insets show the octahedral morphology. **c**, HRTEM image of PtNi shows the selective leaching in the facet region. **d**,**e**, EELS line scans show the thicker Pt shell of $Pt_{1.5}Ni$ relative to PtNi. These results demonstrate that after 25 potential cycles the Ni was still rich near the surface and the thickness of the Pt shell in PtNi was less than that of $Pt_{1.5}Ni$. **f**, STEM image of $PtNi_{1.5}$ shows of the concave structure in $PtNi_{1.5}$ relative to $Pt_{1.5}Ni$ (**d**,**e**, inset), suggesting the selective leaching of Ni in the facets.

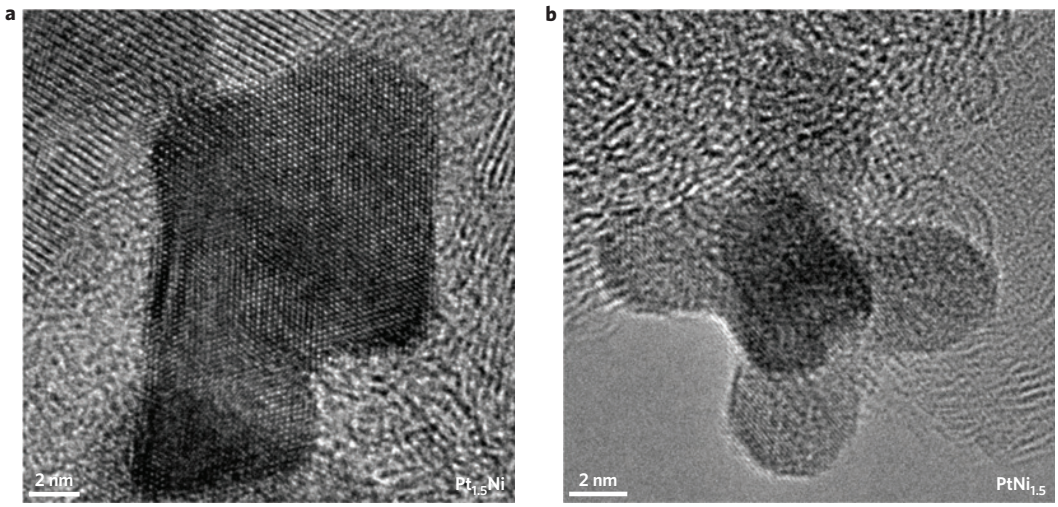

Figure 4 | HRTEM images of Pt_xNi_{1-x} octahedra after stability tests. a, HRTEM image of a $Pt_{1.5}Ni$ octahedral nanoparticle suggests that the nanoparticle basically maintains the octahedral structure after the stability test. **b**, HRTEM image of a $PtNi_{1.5}$ octahedral nanoparticle shows that selective leaching in the facets of the Ni rich $PtNi_{1.5}$ results in the formation of a orthogonal skeleton structure.

varying degrees. The $Pt_{1.5}Ni$ octahedra (Fig. 3d,e) show enhanced Pt shell thicknesses of 5–12 atomic layers. The PtNi catalyst showed a mixed picture, with areas of Ni depletion (arrows in Fig. 3a), but also with regions of higher near-surface Ni content (Fig. 3b at position 0–5 nm). It is conceivable that the Pt-rich frame consisting of corners and edges can delay or even prevent massive leaching of Ni from adjacent areas. Possibly, the high-Ni regions are those where the particle was connected to the support and thus remained intact. The mean shell thickness of the activated PtNi catalyst was estimated to be about 1–4 atomic layers, clearly thinner than that of the $Pt_{1.5}Ni$. The high-resolution TEM (HRTEM) image in Fig. 3c provided a unique direct insight into how the octahedral {111} facets transform during the electrochemical activation. Only the facet centres showed preferential leaching, creating concave steps near the centre of the facet. This is consistent with the Ni enrichment pattern found in the pristine materials. The most striking morphological and structural transformation, however, was observed for the activated $PtNi_{1.5}$ catalyst in the STEM image of Fig. 3f. It shows various activated particles along the ⟨100⟩ zone axis. Clearly visible is a well-developed dark concave shaped region inside the four quadrants spanned by the octahedral main axes. Ni leaching in the facet centres reached deep into the octahedra. This facet preferred dissolution-eliminated {111} facets in favour of {100} facets. Kinetic studies of surface dealloying

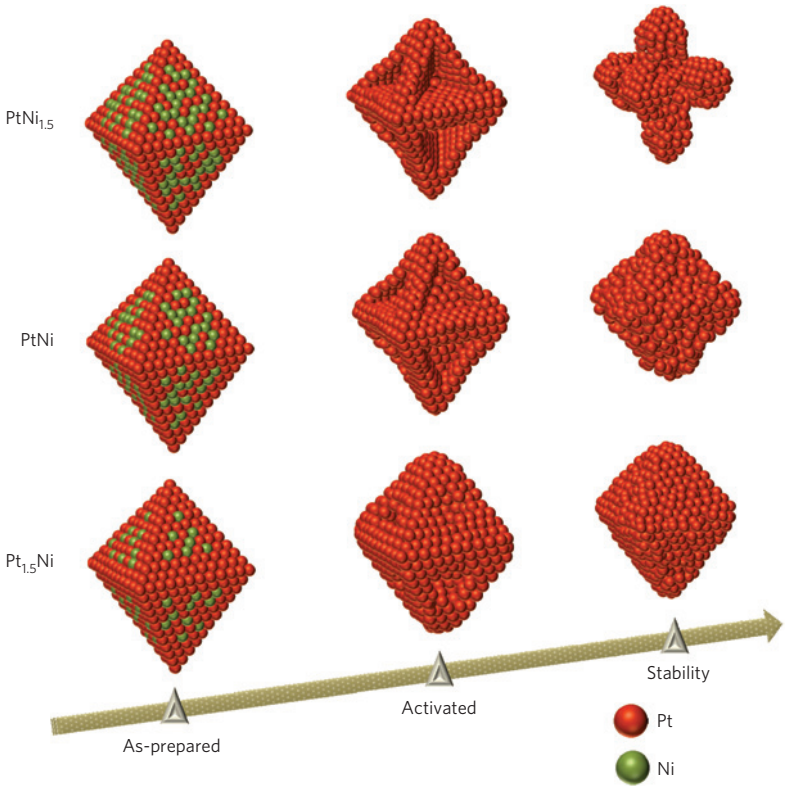

Figure 5 | Morphology and surface structural changes of Pt_xNi_{1-x} octahedra. Schematic representation of the Pt_xNi_{1-x} nanoparticle morphology and surface structure changes after electrochemical surface activation (25 potential cycles) and electrochemical stability tests relative to as-synthesized nanoparticles.

processes on extended, uniform, bulk alloy surfaces revealed a terrace-dissolution mechanism from low-index facets[37]. Although potentially relevant also for the current case, the Ni segregation patterns towards the facet centres seem to play a more important role in explaining the facet-preferred dissolution.

The trends in the ORR activity of the three activated Pt_xNi_{1-x} octahedra in Fig. 2 can now be related to the atomic-scale near-surface composition patterns. Bulk composition is obviously an insufficient predictor and descriptor for surface electrocatalytic activity[38,39]. More suitable for this purpose seems to be the thickness of the Pt-enriched shell[40] (Fig. 3) and the immediate Ni content below the Pt shell. Dealloyed activated PtNi octahedra developed very thin Pt shells along {111} facets with beginning concave topology. At the bottom of the concave pit, Pt {111} facets seem to be stabilized, largely maintaining an octahedral shape. This near-surface structure enables both electronic and surface lattice strain effects to modify the electronic band structure towards a more favourable adsorption and catalysis[22,40–42]. The $Pt_{1.5}Ni$ catalyst, on the other hand, maintained its octahedral shape well, yet developed a very thick Pt overlayer which limited electronic and possibly strain effects, resulting in inferior ORR activities. Activated $PtNi_{1.5}$, finally, has completely transformed its facet structure towards a concave octahedron, losing most of its active {111} facets. Our study underscores how the atomic arrangement of the topmost surface layer, as well as the composition of subsurface layers, affect the catalytic ORR activity irrespective of the detailed composition in the bulk[21,43].

Octahedral Pt_xNi_{1-x} electrocatalysts face a triple challenge of size change, shape change and compositional change in electrochemical environments. We investigated both the stability measured in terms of loss in activity as well as the associated structural changes of the three octahedral catalysts over the course of 4,000 potential cycles. As detailed in Supplementary Fig. S7, the Pt mass activity of the $Pt_{1.5}Ni$, $PtNi_{1.5}$, and PtNi catalysts dropped by 16%, 45% and 66%, respectively, whereas their electrochemical active areas dropped only by 10% and less. Thus, even compared to Pt the $Pt_{1.5}Ni$ octahedra demonstrated outstanding stability. The Ni bulk compositions of the three catalysts decrease slightly down to $Pt_{80}Ni_{20}$ (Supplementary Fig. S5). These results indicate that the ORR activity cannot be attributed to a loss of surface sites or bulk Ni, but again is controlled by the detailed near-surface structure and composition. Although PtNi demonstrated exceptional initial and activated activities, its structural transformations during cycling severely affected its activity. An subsequent atomic-scale study revealed why.

HRTEM investigations (Fig. 4 and Supplementary Fig. S8) revealed a dramatic morphological evolution process for the $PtNi_{1.5}$ catalyst (Fig. 4b), in which the catalyst experienced a complete disappearance of its {111} facets as well as its edges, translating into a dendritic nanoparticle with an orthogonal Pt-rich framework. $Pt_{1.5}Ni$ suffered the least structural transformation during the electrochemical processing and largely maintained its octahedral morphology (Fig. 4a), and its Pt corners and edges seemed to have smoothened out with the electrochemical potential cycling owing to the Pt atomic dissolution/redeposition and rearrangement[44]. The highly active PtNi octahedral catalyst performed poorly after the stability test.

Figure 5 illustrates our morphological findings of the atomic-scale structure–activity–stability study. In Pt_xNi_{1-x} octahedra, Ni has a tendency to segregate into and enrich the {111} facets for all three Ni bulk compositions. Under conditions where Ni selectively leaches, this favours the formation of a concave facet structure lowering the ratio of the active {111} facets. Ni-rich octahedra thereby degrade to Pt-rich skeleton frameworks. Our atomic-scale finding of Ni enrichments and segregations in the {111} facets are important as they also refine a very recently proposed theoretical DFT-based etching model for Pt–Ni nano octahedra[27]. Pt-rich

octahedra withstand the detrimental corrosive conditions much better and can maintain their geometry. The bulk Ni loss is similar for all three catalysts.

In summary, we established that, in contrast to theoretical predictions, a Pt-rich frame (corners and edges)/Ni-rich facet composition profile is prevalent in Pt_xNi_{1-x} octahedra using the STEM-EELS technique. We followed the lifecycle of exceptionally active octahedral Pt_xNi_{1-x} nanoparticle electrocatalysts, monitoring their catalytic activity trajectories along with their compositional, morphological and surface structural evolutions. This yielded unexpected insights into the pristine structure, the activation and degradation of these shape-selective electrocatalysts. Dealloying under electrochemical conditions produced concave octahedral corrosion patterns inside the {111} facets. A delicate balance between the thickness of the resulting Pt shells, the subsurface Ni content and the ratio of remaining {111} facets ultimately determined the maximum ORR activity and governed the pathway to degradation through the continued loss of {111}-oriented facets combined with increasing pure Pt shell thickness. This collapse of the near-surface alloy structure for Ni-rich octahedra affects the surface adsorption of oxygen in a detrimental way and thus finally depresses the ORR activity. However, our study also suggests that Pt-rich Pt–Ni octahedra exhibit relatively high and technologically relevant ORR activities in their activated state with favourable stability.

Methods

Synthesis. $Pt_{1.5}Ni$, PtNi and $PtNi_{1.5}$ octahedra were prepared by modifying a newly developed surfactant-free solvothermal approach[45]. The bulk compositions were controlled by adding an appropriate stoichiometric ratio of starting platinum(II) acetylacetonate [$Pt(acac)_2$] and nickel(II) acetylacetonate [$Ni(acac)_2$] precursors (Alfa Aesar) in a dimethylformamide solvent (Sigma-Aldrich). The mixed solutions in a sealed autoclave were heated from room temperature to 120 °C within 10 min (the heating rate is ~10 °C min^{-1}). The $Pt_{1.5}Ni$, PtNi and $PtNi_{1.5}$ nanoparticles with a fine octahedral structure were synthesized after a reaction of 42 h. Before washing the particles, the carbon support (Vulcan XC-72) was added to the colloid solution. Finally, Pt_xNi_{1-x}/C with a controlled composition was obtained by washing with ethanol/water several times. A detailed description of the experimental method is provided in the Supplementary Information.

Electron microscopy (HRTEM and STEM-EELS)[46]. The surface atomic arrangements were observed by HRTEM on a FEI-Titan 80–300 electron microscope equipped with a spherical aberration (Cs) corrector (CEOS) for the objective lens. The experiment was operated at a voltage of 300 kV using the negative-Cs imaging technique (with Cs set at around ~13 μm and defocus around +6 nm), which allows high contrast and low noise. STEM-EELS experiments were performed in a FEI Titan 80–300 and a FEI Titan 50–300 'PICO' electron microscope operated at 300 and 80 kV. Both microscopes are equipped with a probe corrector (CEOS) and a HAADF detector. '*Z*-contrast' conditions were achieved using a probe semi-angle of 25 mrad and an inner collection angle of the detector of 70 mrad. EELS spectra were recorded with a Gatan image filter Tridiem ERS and Quantum ERS system analysing the Ni $L_{2,3}$-edge and Pt $M_{4,5}$-edge. The energy resolution determined from the full-width at half-maximum of the zero-loss peaks was about 1 eV. For the EELS line profile measurements, both Ni L-edge and Pt M-edge spectra were collected along about 20–30 points across individual nanoparticles with an acquisition time of 1–2 s/spectrum. The relative intensities of the Ni L-edge and Pt M-edge were normalized with respect to their elemental scattering cross sections so that they can be directly related to the number of atoms along the electron beam. More detailed information was reported in reference[46]. Other surface morphology and composition measurements are provided in the Supplementary Information.

Electrochemical measurements. The initial three potential cycles were performed at 100 mV s^{-1} between 0.06 and 1.0 V to roughly allow the dealloying of the surface Ni atoms and obtain the surface voltammetric response. The third one was recorded to estimate the ECSA. The obtained surface was defined as the 'initial' surface. The catalysts were further electrochemical activated by potential cycling between 0.06 and 1.0 V and the 25th potential cycle was recorded to evaluate the ECSA. The stability test was performed between 0.6 and 1.0 V at 50 mV s^{-1} for 4,000 cycles, during which the potential region was changed to 0.06–1.0 V and the scan rate was changed to 100 mV s^{-1} after the 250th, 500th, 1,000th, 2,000th, 3,000th and 4,000th cycles to evaluate the ECSA change.

Considering that the strong interaction between CO_{ad} and surface Pt sites may modify the surface morphology/composition, CO stripping was performed in parallel experiments[33,47]. Before CO-stripping, the electrolyte was saturated with CO by bubbling through the solution for 15 min. The Pt-ECSA was confirmed using CO-stripping to avoid the underestimation of the ECSA owing to the possible suppression of H_{upd} adsorption.

Linear sweep voltammetry measurements were conducted in an oxygen-saturated 0.1 M $HClO_4$ solution by sweeping the potential from 0.06 to 1.05 V at 5 mV s^{-1} (1,600 r.p.m.). Mass and specific activities were studied at 0.9 V, and were depicted as kinetic current densities normalized to the real active surface area and loading Pt mass.

Received 7 December 2012; accepted 19 April 2013; published online 16 June 2013

References

1. Arico, A. S., Bruce, P., Scrosati, B., Tarascon, J. M. & Van Schalkwijk, W. Nanostructured materials for advanced energy conversion and storage devices. *Nature Mater.* **4,** 366–377 (2005).
2. Sasaki, K. *et al.* Highly stable Pt monolayer on PdAu nanoparticle electrocatalysts for the oxygen reduction reaction. *Nature Commun.* **3,** 1–5 (2012).
3. Yu, W. T., Porosoff, M. D. & Chen, J. G. G. Review of Pt-based bimetallic catalysis: From model surfaces to supported catalysts. *Chem. Rev.* **112,** 5780–5817 (2012).
4. Watanabe, M., Tsurumi, K., Mizukami, T., Nakamura, T. & Stonehart, P. Activity and stability of ordered and disordered Co-Pt alloys for phosphoric-acid fuel-cells. *J. Electrochem. Soc.* **141,** 2659–2668 (1994).
5. Rabis, A., Rodriguez, P. & Schmidt, T. J. Electrocatalysis for polymer electrolyte fuel cells: Recent achievements and future challenges. *ACS Catal.* **2,** 864–890 (2012).
6. Debe, M. K. Electrocatalyst approaches and challenges for automotive fuel cells. *Nature* **486,** 43–51 (2012).
7. Wagner, F. T., Lakshmanan, B. & Mathias, M. F. Electrochemistry and the future of the automobile. *J. Phys. Chem. Lett.* **1,** 2204–2219 (2010).
8. Stephens, I. E. L. *et al.* Tuning the activity of Pt(111) for oxygen electroreduction by subsurface alloying. *J. Am. Chem. Soc.* **133,** 5485–5491 (2011).
9. Toda, T., Igarashi, H., Uchida, H. & Watanabe, M. Enhancement of the electroreduction of oxygen on Pt alloys with Fe, Ni, and Co. *J. Electrochem. Soc.* **146,** 3750–3756 (1999).
10. Greeley, J. *et al.* Alloys of platinum and early transition metals as oxygen reduction electrocatalysts. *Nature Chem.* **1,** 552–556 (2009).
11. Snyder, J., Fujita, T., Chen, M. W. & Erlebacher, J. Oxygen reduction in nanoporous metal–ionic liquid composite electrocatalysts. *Nature Mater.* **9,** 904–907 (2010).
12. Liu, Z., Yu, C., Rusakova, I. A., Huang, D. & Strasser, P. Synthesis of Pt_3Co alloy nanocatalyst via reverse micelle for oxygen reduction reaction in PEMFCs. *Top. Catal.* **49,** 241–250 (2008).
13. Stamenkovic, V. R. *et al.* Improved oxygen reduction activity on Pt_3Ni(111) via increased surface site availability. *Science* **315,** 493–497 (2007).
14. Stamenkovic, V. R. *et al.* Trends in electrocatalysis on extended and nanoscale Pt-bimetallic alloy surfaces. *Nature Mater.* **6,** 241–247 (2007).
15. Carpenter, M. K., Moylan, T. E., Kukreja, R. S., Atwan, M. H. & Tessema, M. M. Solvothermal synthesis of platinum alloy nanoparticles for oxygen reduction electrocatalysis. *J. Am. Chem. Soc.* **134,** 8535–8542 (2012).
16. Zhang, J., Yang, H., Fang, J. & Zou, S. Synthesis and oxygen reduction activity of shape-controlled Pt_3Ni nanopolyhedra. *Nano Lett.* **10,** 638–644 (2010).
17. Wu, J. B., Gross, A. & Yang, H. Shape and composition-controlled platinum alloy nanocrystals using carbon monoxide as reducing agent. *Nano Lett.* **11,** 798–802 (2011).
18. Wu, J. *et al.* Truncated octahedral Pt_3Ni oxygen reduction reaction electrocatalysts. *J. Am. Chem. Soc.* **132,** 4984–4985 (2010).
19. Wu, Y., Cai, S., Wang, D., He, W. & Li, Y. Syntheses of water-soluble octahedral, truncated octahedral, and cubic Pt–Ni nanocrystals and their structure–activity study in model hydrogenation reactions. *J. Am. Chem. Soc.* **134,** 8975–8981 (2012).
20. Gasteiger, H. A. & Markovic, N. M. Just a dream-or future reality? *Science* **324,** 48–49 (2009).
21. Gan, L., Heggen, M., Rudi, S. & Strasser, P. Core-shell compositional fine structures of dealloyed Pt_xNi_{1-x} nanoparticles and their impact on oxygen reduction catalysis. *Nano Lett.* **12,** 5423–5430 (2012).
22. Strasser, P. *et al.* Lattice-strain control of the activity in dealloyed core-shell fuel cell catalysts. *Nature Chem.* **2,** 454–460 (2010).
23. Van der Vliet, D. F. *et al.* Mesostructured thin films as electrocatalysts with tunable composition and surface morphology. *Nature Mater.* **11,** 1051–1058 (2012).
24. Colon-Mercado, H. R. & Popov, B. N. Stability of platinum based alloy cathode catalysts in PEM fuel cells. *J. Power Sources* **155,** 253–263 (2006).
25. Wang, D. S., Zhao, P. & Li, Y. D. General preparation for Pt-based alloy nanoporous nanoparticles as potential nanocatalysts. *Sci. Rep.* **1,** 1–5 (2011).
26. Snyder, J., McCue, I., Livi, K. & Erlebacher, J. Structure/processing/properties relationships in nanoporous nanoparticles as applied to catalysis of the cathodic oxygen reduction reaction. *J. Am. Chem. Soc.* **134,** 8633–8645 (2012).

27. Wu, Y. *et al.* A strategy for designing a concave Pt–Ni alloy through controllable chemical etching. *Angew. Chem. Int. Ed.* **51,** 12524–12528 (2012).
28. Oezaslan, M., Heggen, M. & Strasser, P. Size-dependent morphology of dealloyed bimetallic catalysts: linking the nano to the macro scale. *J. Am. Chem. Soc.* **134,** 514–524 (2011).
29. Strasser, P. Dealloyed core-shell fuel cell electrocatalysts. *Rev. Chem. Eng.* **25,** 255–295 (2009).
30. Wang, C. *et al.* Correlation between surface chemistry and electrocatalytic properties of monodisperse Pt_xNi_{1-x} nanoparticles. *Adv. Funct. Mater.* **21,** 147–152 (2011).
31. Wang, G. F., Van Hove, M. A., Ross, P. N. & Baskes, M. I. Monte Carlo simulations of segregation in Pt–Ni catalyst nanoparticles. *J. Chem. Phys.* **122,** 024706 (2005).
32. Urban, K. W. Studying atomic structures by aberration-corrected transmission electron microscopy. *Science* **321,** 506–510 (2008).
33. Van der Vliet, D. F. *et al.* Unique electrochemical adsorption properties of Pt-skin surfaces. *Angew. Chem. Int. Ed.* **51,** 3139–3142 (2012).
34. Colon-Mercado, H. R., Kim, H. & Popov, B. N. Durability study of Pt_3Ni_1 catalysts as cathode in PEM fuel cells. *Electrochem. Commun.* **6,** 795–799 (2004).
35. Antolini, E., Salgado, J. R. C. & Gonzalez, E. R. The stability of Pt-M (M = first row transition metal) alloy catalysts and its effect on the activity in low temperature fuel cells—a literature review and tests on a Pt–Co catalyst. *J. Power Sources* **160,** 957–968 (2006).
36. Chen, S., Gasteiger, H. A., Hayakawa, K., Tada, T. & Shao-Horn, Y. Platinum-alloy cathode catalyst degradation in proton exchange membrane fuel cells: Nanometer-scale compositional and morphological changes. *J. Electrochem. Soc.* **157,** A82–A97 (2010).
37. Snyder, J. & Erlebacher, J. Kinetics of crystal etching limited by terrace dissolution. *J. Electrochem. Soc.* **157,** C125–C130 (2010).
38. Dubau, L., Maillard, F., Chatenet, M., Andre, J. & Rossinot, E. Nanoscale compositional changes and modification of the surface reactivity of Pt_3Co/C nanoparticles during proton-exchange membrane fuel cell operation. *Electrochim. Acta* **56,** 776–783 (2010).
39. Dubau, L. *et al.* Further insights into the durability of Pt_3Co/C electrocatalysts: Formation of 'hollow' Pt nanoparticles induced by the Kirkendall effect. *Electrochim. Acta* **56,** 10658–10667 (2011).
40. Wang, C. *et al.* Design and synthesis of bimetallic electrocatalyst with multilayered Pt-Skin surfaces. *J. Am. Chem. Soc.* **133,** 14396–14403 (2011).
41. Wang, D. *et al.* Structurally ordered intermetallic platinum–cobalt core–shell nanoparticles with enhanced activity and stability as oxygen reduction electrocatalysts. *Nature Mater.* **12,** 81–87 (2013).
42. Zhang, J., Vukmirovic, M. B., Xu, Y., Mavrikakis, M. & Adzic, R. R. Controlling the catalytic activity of platinum-monolayer electrocatalysts for oxygen reduction with different substrates. *Angew. Chem. Int. Ed.* **44,** 2132–2135 (2005).
43. Cui, C. H., Li, H. H., Liu, X. J., Gao, M. R. & Yu, S. H. Surface composition and lattice ordering-controlled activity and durability of CuPt electrocatalysts for oxygen reduction reaction. *ACS Catal.* **2,** 916–924 (2012).
44. Kolb, D. M. Reconstruction phenomena at metal-electrolyte interfaces. *Prog. Surf. Sci.* **51,** 109–173 (1996).
45. Cui, C. *et al.* Octahedral PtNi nanoparticle catalysts: Exceptional oxygen reduction activity by tuning the alloy particle surface composition. *Nano Lett.* **12,** 5885–5889 (2012).
46. Heggen, M., Oezaslan, M., Houben, L. & Strasser, P. Formation and analysis of core–shell fine structures in Pt bimetallic nanoparticle fuel cell electrocatalysts. *J. Phys. Chem. C* **116,** 19073–19083 (2012).
47. Mayrhofer, K. J. J., Juhart, V., Hartl, K., Hanzlik, M. & Arenz, M. Adsorbate-induced surface segregation for core-shell nanocatalysts. *Angew. Chem. Int. Ed.* **48,** 3529–3531 (2009).

Acknowledgements

We thank the Zentraleinrichtung für Elektronenmikroskopie (Zelmi) of the Technical University Berlin for their support with TEM and energy-dispersive X-ray spectra techniques. This work was supported by US DOE EERE award DE-EE0000458 via subcontract through General Motors. P.S. acknowledges financial support through the cluster of excellence in catalysis (UniCat).

Author contributions

P.S. and C.C. conceived and designed the experiments. C.C. carried out the chemical synthesis and the electrochemical experiments and analysed the results. L.G. and M.H. performed the HRTEM and STEM-EELS experiments, evaluated and analysed the results. P.S. and C.C. aggregated the figures and co-wrote the manuscript. All authors discussed the results, drew conclusions and commented on the manuscript.

Additional information

Supplementary information is available in the online version of the paper. Reprints and permissions information is available online at www.nature.com/reprints. Correspondence and requests for materials should be addressed to P.S.

Competing financial interests

The authors declare no competing financial interests.